

In-situ deformation characterization of mesosegregated high-strength low-alloy steel



Shuxia Wang^{a,1}, Chuanwei Li^{a,*,1}, Mengyao Zheng^a, Zhenhua Ye^a, Haozhang Zhong^a,
Daming Tong^b, Lizhan Han^b, Jianfeng Gu^{b,*}

^a Institute of Materials Modification and Modeling, School of Materials Science and Engineering, Shanghai Jiao Tong University, Shanghai 200240, China

^b Shanghai Key Laboratory of Materials Laser Processing and Modification, Shanghai Jiao Tong University, Shanghai 200240, China

ARTICLE INFO

Keywords:

Mesosegregation
in-situ tensile test
Digital image correlation
Tensile deformation behavior
Strain distribution
High-strength low-alloy steel

ABSTRACT

The inhomogeneous microstructures caused by mesosegregation deeply influence the mechanical properties and stability of materials. However, the relationship between tensile deformation and inhomogeneous microstructures has received limited attention. This paper reports an in-depth investigation of the tensile deformation behavior and strain distribution of mesosegregated high-strength low-alloy (HSLA) steel. A multi-scale digital image correlation (DIC) analysis of *in-situ* scanning electron microscopy images reveals that the discrepancies in the tensile deformation behavior are caused by the microstructural discrepancies between the positive segregation zones (PSZs) and negative segregation zones (NSZs). The larger number of crossed-slip bands in the NSZs indicates a more serious plastic deformation caused by the softer microstructures of this zone, *i.e.*, tempered upper bainite and allotriomorphic ferrite. On the contrary, the harder microstructures of the PSZs, *i.e.*, bulk bainite ferrite, tempered martensite, and lower bainite, having fewer crossed-slip bands, display a higher plastic deformation resistance. Additionally, the lower plastic deformation resistance in the NSZs leads to a lower failure threshold and causes a fracture in the NSZs. This work reveals the influence of mesosegregation on deformation behavior and provides the guideline on the post-heat treatment of heavy forgings.

1. Introduction

Recently, the demand for greater efficiency and security in nuclear power plants has driven the use of thicker and stronger high-strength low-alloy (HSLA) steel for larger-diameter pressure reactor vessels (PRVs) [1,2]. Simultaneously, for reliability, PRVs used in high-temperature, high-pressure, and high-irradiation environments require highly stable mechanical properties [3,4]. In this context, mesosegregation is commonly observed in PRVs, bringing inevitable adverse quality effects [5–12]. The main issue is that, with the increasing size and thickness of PRVs, mesosegregation is increasingly harder to avoid. However, it cannot be prevented in heavy forgings [8,13–17]. Hence, it is crucial to understand the relationship between mesosegregation and the mechanical properties of PRVs.

Segregation in PRV steels, caused by the solubility of the different elements in the liquid and solid phase, leads to the expulsion from the solid phase and migration to the liquid phase of solutes such as Mn, Mo, and Ni during solidification [18–21]. Then, the continuous enrichment

of solutes in the liquid phase and depletion in the solid one leads to the formation of dendritic and interdendritic zones, respectively [5,22–25]. Mesosegregation in heavy forgings refers to the visible dendritic patterns generated during the casting solidification of ingots that, after forging and post-heat treatment, appear as a multiform and random distribution of the components. The width and distance of the mesosegregated zones range from 100 μm to 1 mm, *i.e.*, in the mesoscale range. Hence, in heavy forgings, this special segregation should be called mesosegregation, preserving identical positive (PSZs) and negative segregation zones (NSZs).

Among the main mechanical properties of heavy structural components, the tensile deformation behavior, which measures the yield and tensile strength of materials, is undoubtedly one of the most important parameters. In particular, strain anisotropy, one of the key factors to mechanical properties, is detrimental to the mechanical behavior of PRV because it is caused by microstructural inhomogeneities [26]. There are several studies on the effect of inhomogeneous microstructures on tensile deformation, such as band microstructures in steel

* Corresponding author at: Institute of Materials Modification and Modeling, School of Materials Science and Engineering, Shanghai Jiao Tong University, Shanghai 200240, China.

E-mail addresses: li-chuanwei@sjtu.edu.cn (C. Li), gujf@sjtu.edu.cn (J. Gu).

¹ Contributed equally to this work.

[6,26–35]. It has been claimed that band microstructures would induce the strain partition during the deformation and further result in mechanical properties' anisotropy of inhomogeneous materials. However, the effect of inhomogeneous microstructures has been rarely discussed from the viewpoint of mesosegregation inside a sample. Furthermore, the effect of microstructural discrepancies on the deformation mechanism, still disputed in literature [14,21,33,36–38], lacks systematic investigation. Thus, it is essential to determine the dominant deformation micromechanisms of the different microstructures in meso-segregated HSLA steel.

This paper aims at providing new insights into the tensile deformation behavior and strain distribution of mesosegregated HSLA steel under a lower strain rate. Full-field strain measurements were performed by *in-situ* scanning electron microscopy (SEM) using the digital image correlation (DIC) method [32,33,39–42]. DIC method (post-processing software: Vic-2D 6) was used to analyze the relative displacement of the corresponding two gauge points between the adjacent pictures shooting by the SEM during the tensile test. Different relative displacements indicate different deformation degrees, which in turn indicate different strain concentrations, reflecting the relationship between strain distribution and microstructures. Therefore, the discrepancies of the strain distribution in the PSZs and NSZs during the tensile deformation stage could be clarified. Besides, this paper could also provide a method to predict the tensile strain distribution of a sample in the elastic and plastic deformation stages.

2. Materials and experimental methods

2.1. Sample preparation

The spatial properties of mesosegregation, such as its direction and shape, constitute a complex problem in common forgings [43]. To simplify it, a directional and uniformly shaped mesosegregation is required. Hence, the mesosegregated HSLA steels used in our experiments were non-homogenized ring-shaped heavy forgings. Table 1 lists the average chemical composition of the steels studied in this paper. The temperature of A_{c1} and A_{c3} were measured 732 °C and 807 °C, respectively, at a heating rate of 0.05 °C/s and using a dilatometer. The samples were air-cooled after austenitization at 940 °C for 5 h and tempered at 650 °C for 5 h before cooling to room temperature in the furnace [44].

The geometry and orientation of the tensile sample are schematically shown in Fig. 1(a). The tensile sample had a thickness of 0.2 mm, a gauge width of 2 mm, and a length of 4 mm. The gauge region of these samples had a curve radius to ensure strain localization and necking at the center of the gauge region.

Because the diameter required for the speckle points is different at each scale, different kinds of speckle points are disposed on the tensile samples to match the different scales. For the speckle pattern of the macroscale characterization, the sample surface was sprayed with vaporous black paint for 12 h, obtaining a paint speckle pattern with a diameter of approximately 10 μm. The speckle pattern used for the microscale characterization was obtained by electroplating In on the tensile sample surface in a water bath at 35 °C for 1 min. The diameter of the In speckle points was approximately 1 μm.

2.2. *In-situ* tensile tests and strain measurement

The sample was installed on a special designed *in-situ* tensile stage

Table 1
Chemical composition (wt%) of the mesosegregated HSLA steel sample.

Steel state	C	Mn	Mo	Ni	Cr	Si	Al	Cu	P	Fe
As-received	0.20	1.42	0.49	0.86	0.18	0.18	0.014	0.03	0.003	bal.

(MICROTEST 5kN watercooled, Gatan, United Kingdom) and then placed into field-emission SEM (LYRA3 GMU, TESCAN, Czech Republic). The main parameters for the SEM macroscale *in-situ* tensile characterization were the following ones: high voltage: 20 kV; detector: secondary electron detector; work distance: 30 mm; magnification: 30×; cycle time: 20.5 s. The tensile testing rate was 0.1 mm/min, and SEM images of the sample were captured at every cycle during loading [32]. All images obtained were numbered in chronological order, and the first image was selected as the reference one. Then, DIC [45] (Vic-2D, Correlated Solutions, USA) was used to measure the relative displacements of the other images concerning the reference one. The images captured before and after deformation were inputted into the software, and after setting the analysis area and parameters, the displacements in the x and y direction were calculated differentially to obtain normal strains ϵ_{xx} and ϵ_{yy} in the x and y directions, respectively, and shearing strain γ_{xy} . Then, the output data were used in the 2D equivalent strain formula, written as:

$$\bar{\epsilon} = \sqrt{\frac{2}{3} \left[\left(\frac{2}{3} \epsilon_{xx} - \frac{1}{3} \epsilon_{yy} \right)^2 + \left(\frac{2}{3} \epsilon_{yy} - \frac{1}{3} \epsilon_{xx} \right)^2 + \left(\frac{1}{3} \epsilon_{xx} + \frac{1}{3} \epsilon_{yy} \right)^2 + \frac{1}{2} \gamma_{xy}^2 \right]}, \quad (1)$$

2.3. Microstructure characterization

The microstructures of the PSZs and NSZs were characterized using optical microscopy (OM, Axio Observer A1, Zeiss, Germany), SEM, and electron back-scattered diffraction (EBSD, NordlysMax3, Oxford Instruments, United Kingdom). For OM and SEM characterization, the samples were mechanically polished and etched by a solution of 4% nital. For EBSD measurements, the sample was polished using 50 nm colloidal silica particles (nanochemical-mechanical VibroMet polishing, Buehler, USA) for 2 h after mechanically polishing to obtain a surface roughness of 0.5 μm. The EBSD measurements were obtained by SEM using an EBSD fast acquisition system operating at 20 kV/4 nA with a sample tilt of 70°, the working distance of 9 mm, and step size of 0.2 μm. The captured data was post-processed using the Channel 5 software package (Oxford Instruments, United Kingdom). Electron-probe microanalysis (EPMA, EPMA-1720, Shimadzu, Japan) was conducted to detect discrepancies in the elemental concentrations of the PSZs and NSZs. The hardness of the microstructures was tested by the indentation method using the microhardness tester (Fischer HM2000) with a load from 0 to 500 mN. Then the analysis of the relationship between the load and indentation depth could calculate the microhardness of microstructures.

3. Results and discussion

3.1. Mesosegregation and microstructure

The mesosegregated HSLA steel used in this study was taken from a PRV ring heavy forging and cut in cubic shape. Fig. 1(a) displays an image of the cubic sample after polishing and etching of three faces sharing a vertex. A schematic of the *in-situ* tensile test sampling in the 3D mesosegregation distribution model is presented in Fig. 1(a). Since the sample thickness as 0.2 mm is far thinner than the standard sample thickness, which disobeys the tensile sample size standard and probably could not presents the standard tensile curve. Furthermore, the 3D mesosegregation distribution inside the tensile sample could be reduced to that of a 2D one due to the 0.2 mm thickness. As observed, the mesosegregation bands in the tensile sample are vertically distributed in the load direction. The elemental concentration in the selected zone of the tensile sample shown in Fig. 1(b) was detected by EPMA. As seen, C, Mn, Mo, and Ni are abundant in the dark regions (PSZs) and sparse in the light ones (NSZs).

Fig. 1(c) and (f) display OM images of the PSZ and NSZ marked in

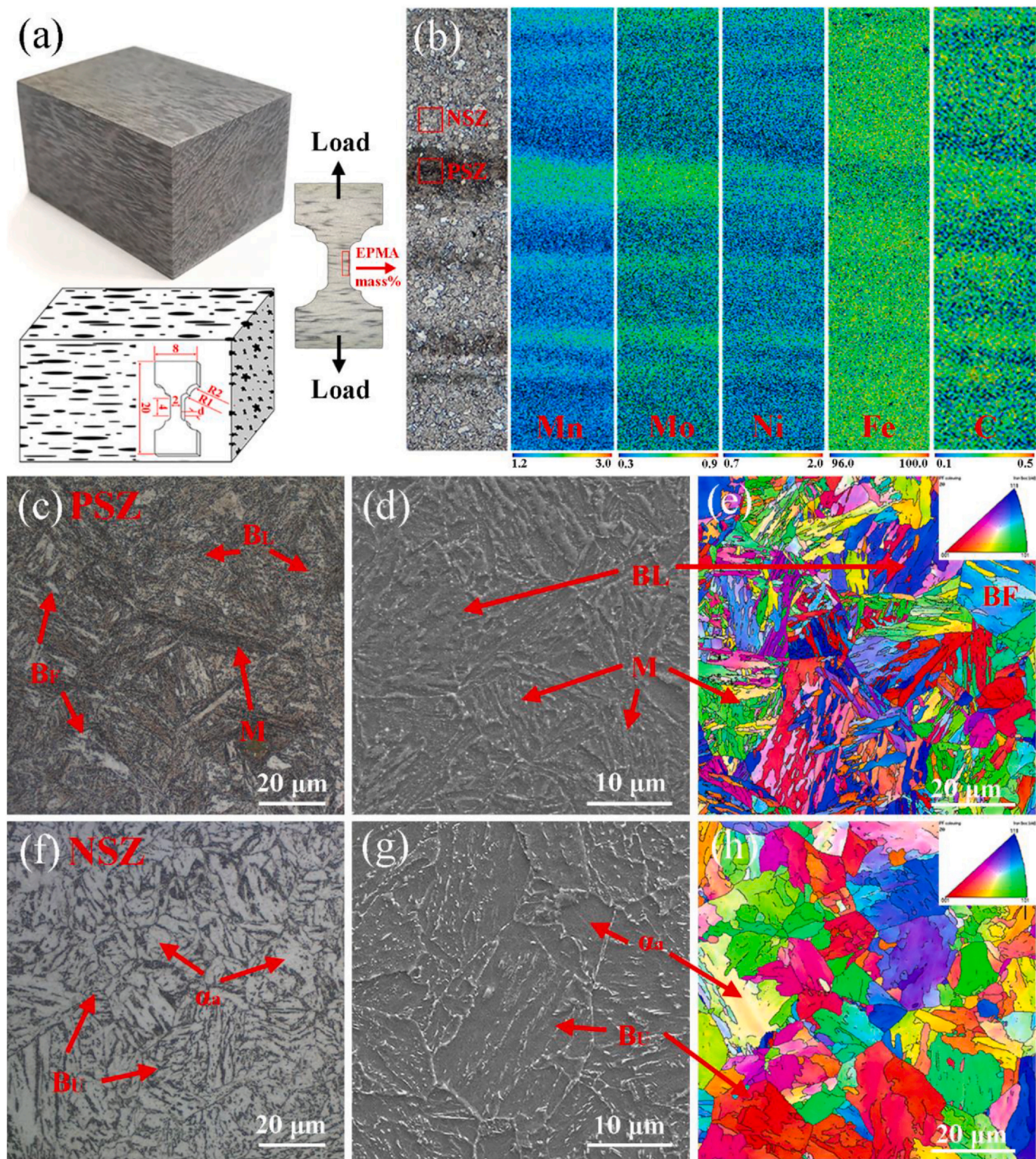


Fig. 1. (a) Schematic of the sampling of the mesosegregated materials. (b) microhardness results of the PSZ and NSZ. (c) EPMA results of the selected area of the tensile sample. Characterization of the microstructures in the (d-f) PSZ and (g-i) NSZ marked in (b).

Fig. 1(b). Generally, at the same cooling speed, a higher element concentration in the PSZ leads to higher hardenability during quenching. Therefore, as shown in Fig. 1(c), the black and dark-grey regions of the PSZ are microstructures of bulk bainite ferrite (B_F), tempered martensite (M), and tempered lower bainite (B_L), respectively. However, it is not easy to identify M and B_L after tempering, especially by OM, because small and uniformly shaped carbides precipitate simultaneously

from the ferrite matrix in both M and B_L during tempering, as confirmed by their similar carbide content [43,44,46]. Also, Fig. 1(d) shows the corresponding SEM image, in which the materials can be distinguished by their different lath width. The ferrite laths of M appear as narrow and long parallel needles, whereas the ferrite laths of B_L appear as wide and short parallel feathers. Besides, as shown in Fig. 1(e), the differences between the M and B_L of the PSZ could be identified in the EBSD

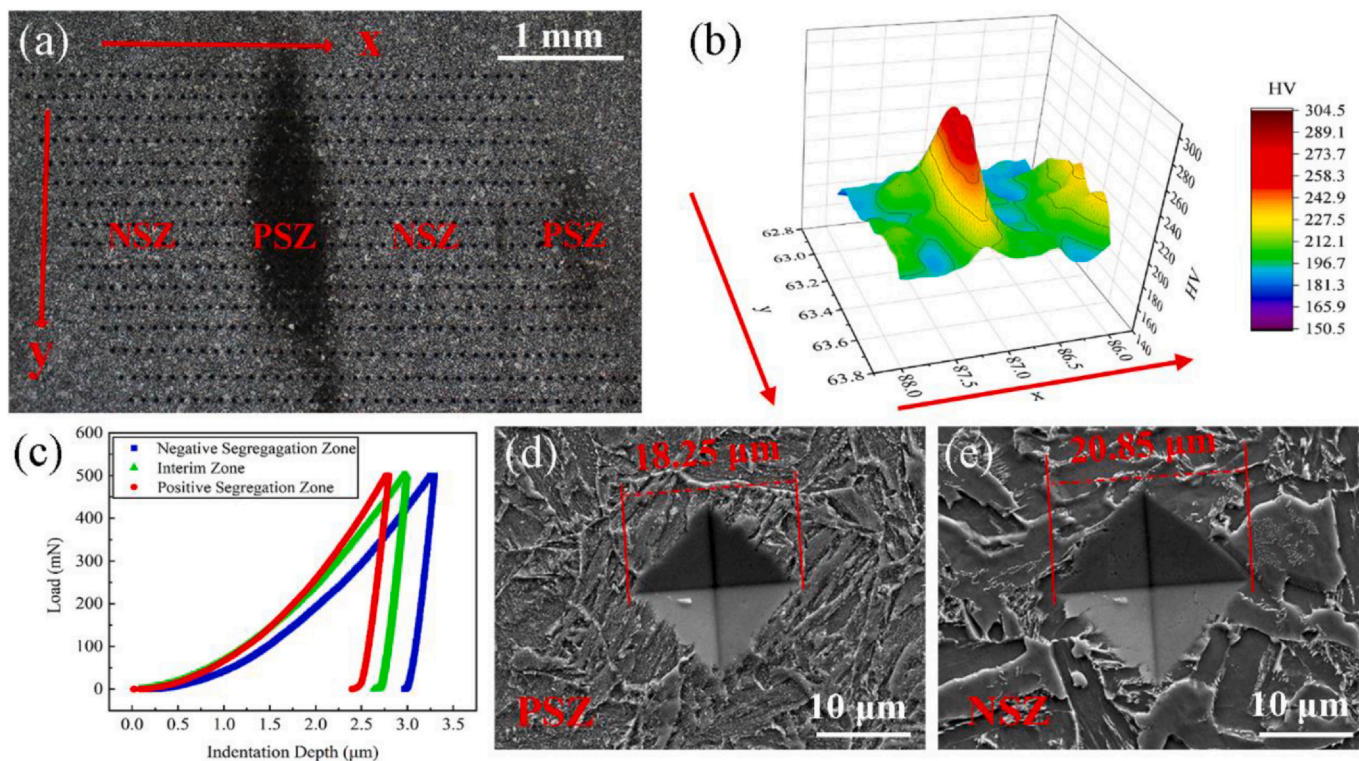


Fig. 2. Microhardness results of the microstructures in PSZ and NSZ. (a) OM image of the microhardness indentation matrix across the PSZ and NSZ. (b) Three-dimensional distribution graph of the matrix's microhardness value. (c) Load curve of the selected microhardness indentation in the PSZ, interim zone, and NSZ. (d) and (e) SEM images of the microhardness indentation selected from the PSZ and NSZ.

inverse pole figures (IPF) map. As seen, the misorientation is higher between the laths of M than between those of B_L . That is, the lath boundary density is higher for M than B_L , which indicates that more energy is stored in M.

On the contrary, the lower elemental concentration in the NSZ results in lower hardenability. As shown in Fig. 1(f-g), the microstructures in the NSZ are tempered upper bainite (B_U) and sparse allotriomorphic ferrite (α_a). Carbides precipitated along the laths boundaries of B_U and coarsened during tempering [44,46]. Furthermore, the black carbides stacked at the boundaries of primary austenite grains are decomposed from the M/A islands during tempering [44,46]. As shown in Fig. 1(h), the IPF map displays the misorientation and effective grain size of the microstructures of the NSZ. Here, the B_U laths are wider and their misorientation is smaller than in the PSZ. The spatial variations of microhardness of the PSZs and NSZs caused by mesosegregation after the austenitization and tempering were also observed.

As shown in Fig. 2(a), a two-dimensional microhardness matrix is indented across the PSZ and NSZ by the microhardness tester to present intuitive hardness variations. In particular, the matrix's microhardness value distribution in Fig. 2(a) is displayed by a three-dimensional graph (Fig. 2(b)). The undulating hills reveal the stark spatial variations of the microhardness in the PSZ and NSZ, and the towering peaks and low valleys corresponding to the PSZs and NSZs, respectively. Besides, the average microhardness value in the PSZs (240 HV) is higher than that in the NSZs (180 HV). On the other hand, the microhardness indentation test provides the corresponding load curve in each indentation, and the representative load-depth curve in the PSZ, NSZ, and the interim zone were analyzed in Fig. 2(c). Indentation depth in the PSZ is smaller than that in the NSZ at the same load, which indicates that the microstructure's resisting deformation ability in the PSZ, is stronger than that in the NSZ. Furthermore, Fig. 2 (b) and (c) show the SEM images of the indentations in the PSZ and NSZ, which present that the diagonal line of the indentation in the PSZ (18.25 μm) is smaller than that in the NSZ (20.85 μm) after suffering the maximum load (500 mN). It could also

provide the other evidence to the stronger resisting deformation ability and higher microhardness of the microstructures in the PSZ.

3.2. Macro-DIC characterization

3.2.1. Strain distribution near the tensile yield stage

As shown in Fig. 3(a1), the stress-strain curve of the macro-DIC test indicates that the yield strength is approximately 350 MPa and the corresponding strain is 1.9%, with a tensile strength of approximately 440 MPa. In the macro-DIC characterization, the whole gauge area of the tensile sample was selected as the region of interest (ROI). Fig. 3(a1-f1) show the calculated equivalent strain distribution maps of the ROI from strain 0 to 4.74%, which is near the tensile yield stage. A redpoint indicating the corresponding tensile stage is marked in the tensile curves. Firstly, Fig. 3(a1) shows that the equivalent strain distribution is 0 in the whole ROI before the tensile test. It should be noticed that the 180 MPa value observed at 0% strain includes the preload force before the test, which does not influence the tensile curve. Secondly, at the elastic deformation stage of Fig. 3(b1), a slight, inhomogeneous distribution of the equivalent strain is observed in the ROI.

As shown in Fig. 3(c1-f1), the inhomogeneity became increasingly evident after the yield point, which is probably related to the inhomogeneous distribution of microstructures caused by mesosegregation. To verify this, as shown in Fig. 3(a2-f2), the maximum equivalent strain fields in the ROI are extracted from the equivalent strain distribution maps and placed at the corresponding tensile sample location. As seen, all higher equivalent strain fields belong to the NSZ, which indicates a severe deformation of the microstructures in this zone. Additionally, the inhomogeneous equivalent strain distribution suggests the presence of plastic deformation discrepancies in the PSZ and NSZ microstructures. Meaningfully, the calculated strain map evidences the strain distribution difference between the PSZ and NSZ, indicating a strong relationship between the microstructures and deformation.

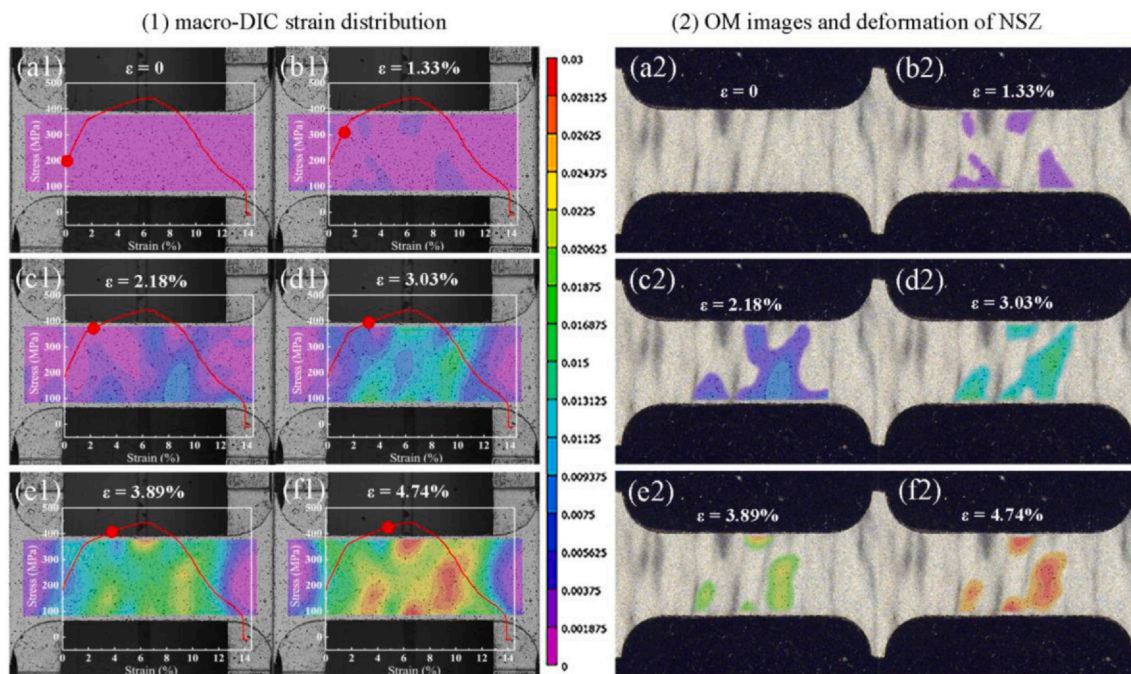


Fig. 3. Equivalent strain maps from the uniaxial tensile test using (1) macro-DIC and (2) SEM images of the ROI at strain (a) 0%, (b) 1.33%, (c) 2.18%, (d) 3.03%, (e) 3.89%, and (f) 4.74% near the tensile yield stage.

3.2.2. Deformation analysis before cracking

To observe the strain concentration near the tensile necking stage clearly, four representative NSZs in the ROI are circled by red dash lines and numbered from 1 to 4. As shown in Fig. 4(a1), the circled NSZs are not only the areas with higher strain concentrations of Fig. 3(f1), but also the reference areas of the strain maps shown in Fig. 4(b1-f1). Fig. 4(b1) shows the equivalent strain distribution of the ROI at 5.6% strain. The strain in the circled NSZs is still higher than in other areas. Particularly, the calculated equivalent strain in the first circle, which is emphasized by a red arrow, is the highest one in the four circles.

As shown in Fig. 4(c1), the equivalent strain in the whole ROI increases when the strain is 6.45%, with the highest strain found in the first circle. Furthermore, the equivalent strain discrepancies between the PSZ and NSZ are larger at strain 6.45% than at 5.60%, which indicates that the equivalent strain increases faster in the NSZ than in the PSZ. Therefore, at strain 7.30%, the equivalent strain discrepancies become larger, and there appears a small crack initiation point in the first circle.

As shown in Fig. 4(e1-f1), the equivalent strain concentrated highly in the crack point after this appeared during the tensile test. The yellow

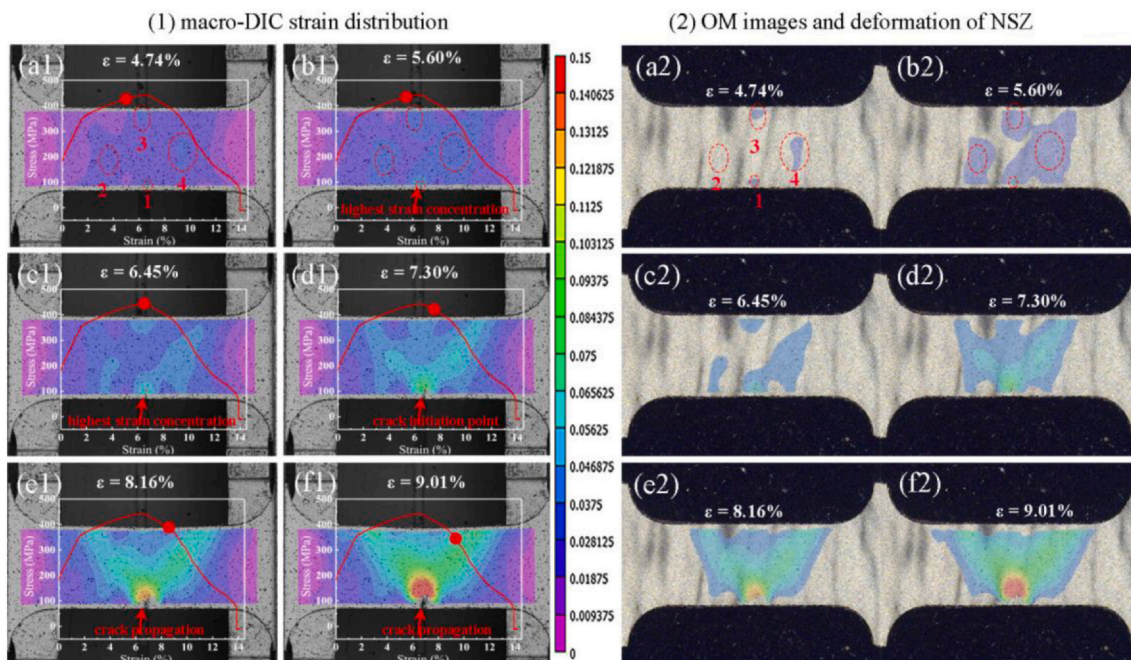


Fig. 4. Equivalent strain maps and crack analysis of the ROI. (1) equivalent strain maps and (2) SEM image of the selected (1) NSZ at strain (a) 4.74%, (b) 5.60%, (c) 6.45%, (d) 7.30%, (e) 8.16%, and (f) 9.01% in the tensile necking stage.

and green areas in the NSZ indicate greater plastic deformation in the necking stage, though higher precision methods would be needed for further characterization. Importantly, the calculated strain map could be used to predict the crack initiation point. The higher the strain concentration, the higher the probability of crack initiation. Hence, the map could also reveal the influence of the mesosegregation distribution on the crack initiation point in the tensile necking stage.

Similarly, as shown in Fig. 4(a2-f2), to investigate the relationship between the equivalent strain and mesosegregation, higher equivalent strain fields in the ROI are extracted from the equivalent strain distribution maps and placed in the corresponding location of the tensile sample. As seen in Fig. 4(a2-c2), from the work-hardening stage to the necking point, higher equivalent strain fields are located in the NSZ. After the necking point, the equivalent strain increases sharply, covering nearly the whole ROI, so that the mesosegregation distribution cannot be distinguished. However, the mesosegregation distribution is related to the contour line of the equivalent strain, which widens in the NSZ and shrinks in the PSZ. This indicates that the microstructures in the PSZ hinder the strain extension and those in the NSZ concentrate strain during severe plastic deformation.

3.3. Micro-DIC analysis

3.3.1. Strain distribution in the PSZ and NSZ

Fig. 5 displays the deformation behavior of mesosegregation during the tensile test with a new sample observed by micro-DIC. As shown in Fig. 5(a), the selected mesosegregation zone analyzed during the DIC related tensile test contains both the PSZ and NSZ. The tensile test was conducted at intervals of 0.1 mm, pause the measurement at each step, as highlighted by the vertical lines on the tensile curve. The equivalent strain maps corresponding to each step are displayed in Fig. 5(d).

At tensile displacement 0.1 mm, in the elastic deformation stage, it can be observed that the strain in both the PSZ and NSZ is below

0.00625, with a negligible discrepancy. However, when the tensile displacement is 0.2 mm, which is over the yield point and in the work-hardening stage, the equivalent strain discrepancy between the PSZ and NSZ is observed. As seen from the color scale, the average equivalent strain value in the PSZ (purple/blue areas) is approximately 0.01, and the value in the NSZ (blue/green) is approximately 0.04. Hence the strain difference between the PSZ and NSZ is 0.03. The higher average equivalent strain value in the NSZ with respect to the PSZ indicates a higher deformation degree of the microstructures in the former.

When the tensile displacement increases to 0.4 mm, which is near the tensile necking stage, the equivalent strain in both the PSZ and NSZ increased and remaining higher in the NSZ. The equivalent strain reaches a maximum of 0.1 in the NSZ, whereas it is approximately 0.04 in the PSZ, with the difference reaching 0.06. Furthermore, a lot of crossed-slip bands are observed in the equivalent strain map. However, the number of crossed-slip bands in the NSZs is more than that in the PSZs. In terms of the microstructures' influence factors, the larger number of crossed-slip bands in the NSZs indicates a more serious plastic deformation caused by the softer microstructures of this zone, *i.e.*, tempered B_{II} and α_a . On the contrary, the harder microstructures of the PSZs, *i.e.*, B_F , tempered M, and B_L , having fewer crossed-slip bands, display a higher plastic deformation resistance.

Then, at a tensile displacement of 0.6 mm, after the necking stage, the red region in the NSZ enlarges, indicating an increasing plastic deformation degree. However, the blue and green colors in the PSZ show only a slight variation, which indicates small changes in the equivalent strain in the PSZ. Additionally, as seen in the SEM image of the last step, shown in Fig. 5(c), the surface relief in the NSZ is greater than that in the PSZ at 0.7 mm displacement, confirming a large deformation degree in the NSZ. Hence, it can be concluded that the deformation mainly increased in the microstructures of the NSZ, and remained nearly constant in those of the PSZ. This reflects the strain partitioning of the mesosegregated microstructures.

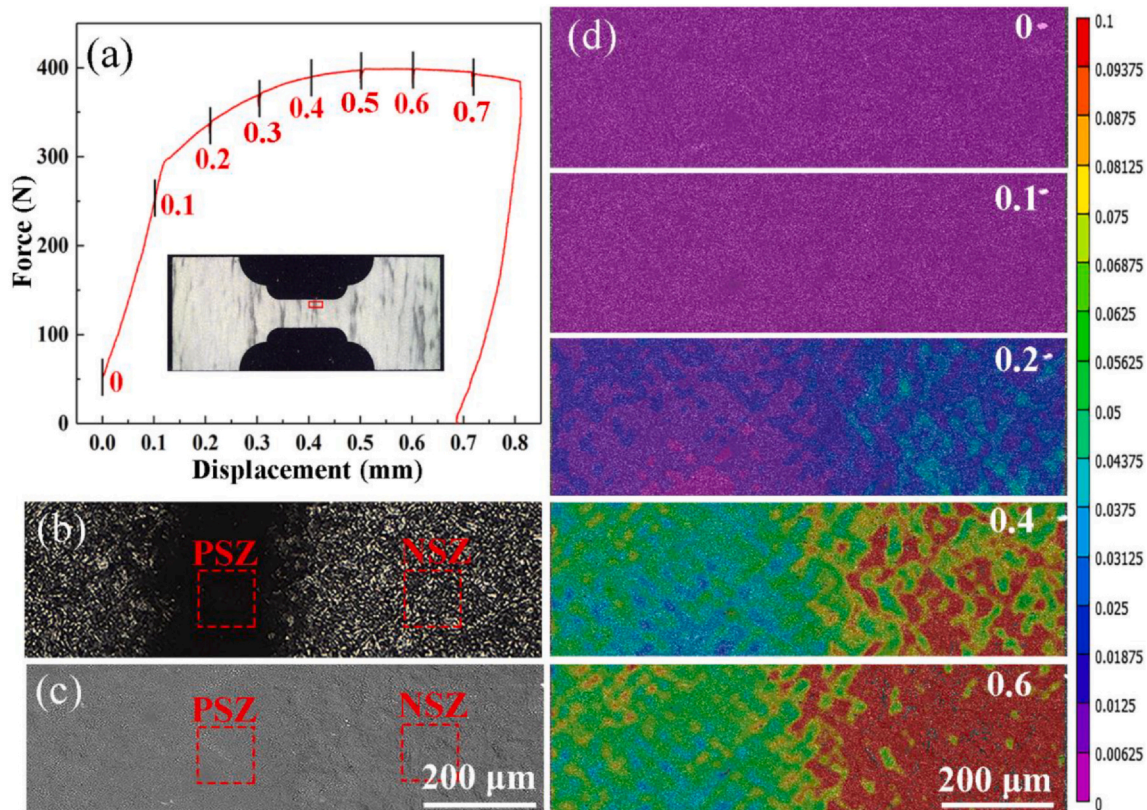


Fig. 5. Micro-DIC analysis of deformation behavior in the mesosegregation. (a) Tensile sample and tensile curve at displacement intervals of 0.1 mm. (b) OM and (c) SEM images of the selected mesosegregated zones of the tensile sample surface. (d) Equivalent strain maps at each displacement.

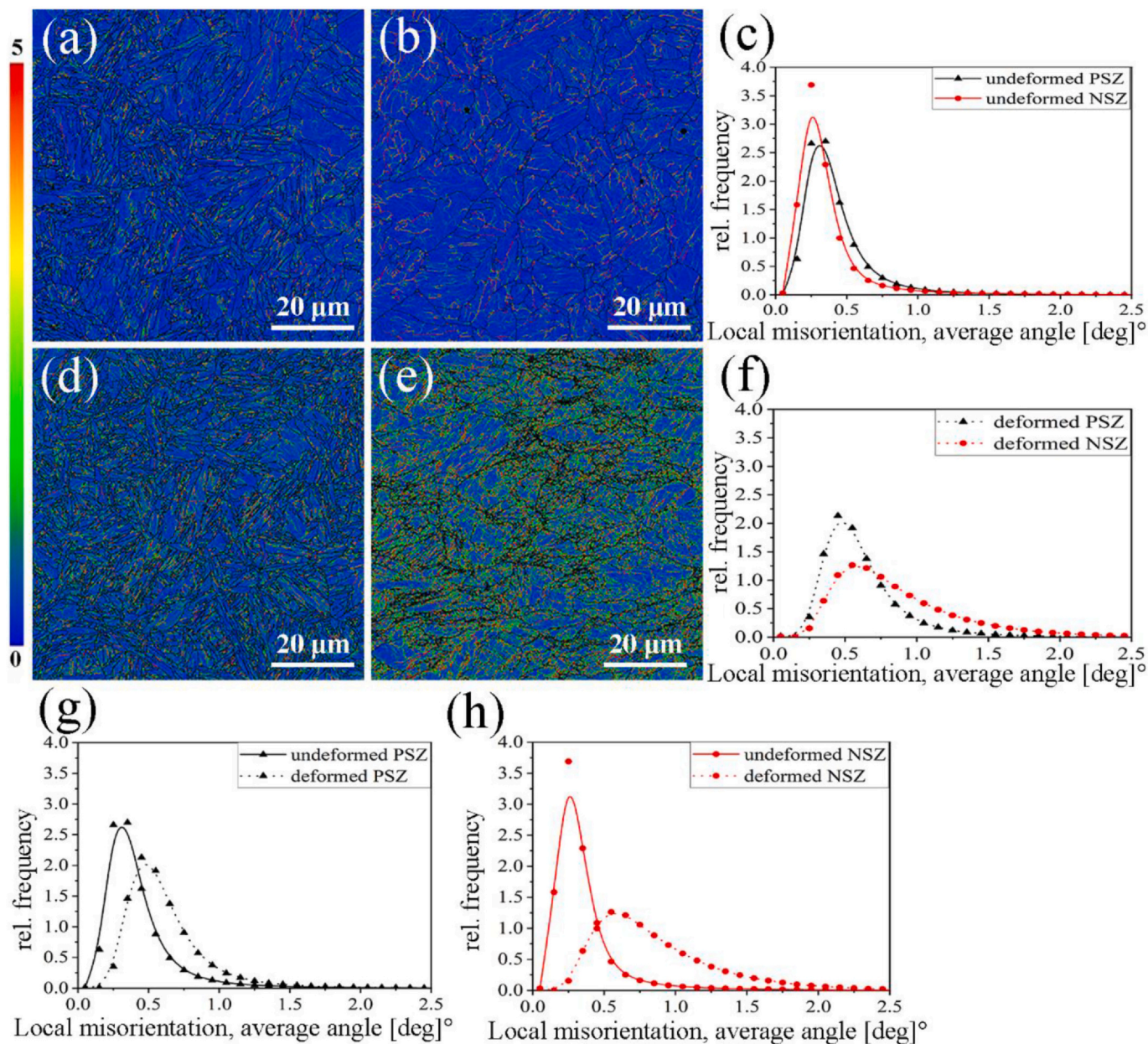


Fig. 6. LM maps of the PSZ and NSZ through the tensile deformation. LM maps of the undeformed (a) PSZ and (b) NSZ, and (c) statistical graph of the data extracted from these LM maps of the deformed (c) PSZ and (d) NSZ, and (f) statistical graph of the data extracted from these. Statistical graphs of the data extracted from the LM maps of the PSZ and NSZ (g) before and (h) after the tensile deformation.

3.3.2. Deformation degree analysis before and after the test

Fig. 6 shows a comparison of representative local misorientation (LM) maps of the PSZ and NSZ, evidencing their deformation differences. Fig. 6(a-b) show the LM maps of the undeformed PSZ and NSZ and Fig. 6(c) summarizes the statistical distributions of local misorientations. It can be seen that the local misorientations of the microstructures in the NSZ are relatively lower ($M_{ave} = 0.36^\circ$, $M_{peak} = 0.25^\circ$) than that of the PSZ ($M_{ave} = 0.43^\circ$, $M_{peak} = 0.35^\circ$). Although they do not represent absolute strains at these locations, the strain components are calculated using the changes in misorientation, and thus the variations in the strain components are caused by variations in the misorientation and its frequency.

The misorientation tends to be large near grain boundaries, and because the narrower martensite laths in the PSZ provide more grain boundaries, a larger misorientation is associated to the PSZ. Furthermore, it is well known that the relative frequencies of higher

misorientations increase with increasing high-angle density, causing a net strain increase [47]. Hence, the difference in the local misorientation average and peak values in the undeformed PSZ and NSZ is attributed to their microstructure.

The variations in lath width imposed some changes to the data processing that caused an increase in the frequencies of higher misorientations. Because of this, the deformation analysis of the PSZ and NSZ was modified. Therefore, as shown in Fig. 6(d-e), the local misorientation maps of the deformed PSZ and NSZ were analyzed, evidencing severer deformation after tensile testing. The statistical graph in Fig. 6(f) reveals that the local misorientation of the deformed NSZ has a relatively higher value ($M_{ave} = 0.87^\circ$, $M_{peak} = 0.55^\circ$) than that of the PSZ ($M_{ave} = 0.62^\circ$, $M_{peak} = 0.45^\circ$). It is commonly believed that heavily deformed areas in the microstructures are related to high values of the local misorientation. Hence, the local misorientation average and peak values of the deformed NSZ indicate greater accumulation of

plastic deformation work.

Besides, the statistical graphs of Fig. 6(g-h) indicate that the local misorientation distribution of the undeformed microstructures is transferred to the deformed microstructures in both the PSZ and NSZ. This results in a higher local misorientation in the deformed microstructures and causes deformation in not only the PSZ but also the NSZ. Supporting this, Fig. 6(g) shows the local misorientation discrepancies between the undeformed and deformed PSZ ($\Delta M_{ave} = 0.19^\circ$, $\Delta M_{peak} = 0.1^\circ$). The microstructures in the PSZ are mainly M and B_L, which have high grain-angle density. Hence, the deformation of the microstructures in the PSZ is lower when a tensile force is applied, implying a greater ability to store strain energy. As shown in Fig. 6(g), the local misorientation differences in the PSZ are small, which indicates the formation of fewer grain boundaries in the PSZ. In contrast, Fig. 6(h) shows the local misorientation differences between the undeformed and deformed NSZ ($\Delta M_{ave} = 0.51^\circ$, $\Delta M_{peak} = 0.3^\circ$). The microstructures in the NSZ are mainly B_U, having a high lath width and low grain boundary density. The higher average misorientation (0.51°) in the NSZ with respect to the PSZ means that more grain boundaries are formed during the plastic deformation. It also implies a higher deformation degree and lower strain energy storage ability of the microstructures in the NSZ.

4. Conclusions

In this study, the tensile deformation and the differences of strain distribution in the PSZ and NSZ of mesosegregated HSLA steel were investigated by *in-situ* tensile testing, from which the following conclusions were obtained:

1. The distribution of PSZs and NSZs in the ROI influences the tensile deformation behavior of the tensile sample. The equivalent strain differs between the PSZ and NSZ, with a higher strain found in the NSZ.
2. The deformation resistance of the microstructures in the NSZ is lower than that in the PSZ. Plastic deformation occurs more frequently in the microstructures of the NSZ, reaching the damage threshold and inducing the earlier failure.
3. The microstructures in the PSZ are tempered martensite, lower bainite, and bainite ferrite, which have low lath width and large misorientation. These microstructures hardly generate crossed-slip bands and cause the higher deformation resistance of the PSZ. In contrast, the microstructures in the NSZ are tempered upper bainite and allotriomorphic ferrite, which have high lath width and small misorientation. It is easier for these microstructures to generate crossed-slip bands, which causes the lower deformation resistance of the NSZ.
4. This study has provided a multi-scale method for the visualization of microstructural factors as resists deformation, and predicts the tensile strain distribution of a sample in the elastic and plastic deformation stages.

Declaration of Competing Interest

We declare that we do not have any commercial or associative interest that represents a conflict of interest in connection with the work submitted.

Acknowledgments

This work was financially supported by the National Natural Science Foundation of China (Grant No. 51801126), and the National Key Research and Development Program of China (Grant No. 2018YFA0702905).

References

- [1] S.J. Zinkle, G.S. Was, Materials challenges in nuclear energy, *Acta Mater.* 61 (2013) 735–758.
- [2] P. Yvon, F. Carré, Structural materials challenges for advanced reactor systems, *J. Nucl. Mater.* 385 (2009) 217–222.
- [3] T. Toyama, N. Tsuchiya, Y. Nagai, A. Almazouzi, M. Hatakeyama, M. Hasegawa, T. Ohkubo, E. Van Walle, R. Gerard, Irradiation-induced changes of the atomic distributions around the interfaces of carbides in a nuclear reactor pressure vessel steel, *J. Nucl. Mater.* 405 (2010) 177–180.
- [4] M.K. Miller, K.F. Russell, M.A. Sokolov, R.K. Nanstad, APT characterization of irradiated high nickel RPV steels, *J. Nucl. Mater.* 361 (2007) 248–261.
- [5] S. Hong, J. Song, M.-C. Kim, K.-J. Choi, B.-S. Lee, Effects of microstructural variation on Charpy impact properties in heavy-section Mn-Mo-Ni low alloy steel for reactor pressure vessel, *Met. Mater. Int.* 22 (2016) 196–203.
- [6] M. Ahmed, I. Salam, F.H. Hashmi, A.Q. Khan, Influence of banded structure on the mechanical properties of a high-strength maraging steel, *J. Mater. Eng. Perform.* 6 (1997) 165–171.
- [7] T. Michler, Y. Lee, R.P. Gangloff, J. Naumann, Influence of macro segregation on hydrogen environment embrittlement of SUS 316L stainless steel, *Int. J. Hydrog. Energy* 34 (2009) 3201–3209.
- [8] G. Yan, L. Han, C. Li, X. Luo, J. Gu, Effect of macrosegregation on the microstructure and mechanical properties of a pressure-vessel steel, *Metall. Mater. Trans. A* 48 (2017) 3470–3481.
- [9] O.V. Peresadenko, I.N. Logozinskii, S.B. Nikitin, I.A. Smolii, N.A. Marenkov, Influence of ingot homogenization on the impact properties of 4X5MΦC steel strip, *Steel Translation* 42 (2013) 728–729.
- [10] C. Maidorn, D. Blind, Solidification and segregation in heavy forging ingots, *Nucl. Eng. Des.* 84 (1985) 285–296.
- [11] J.T. Kim, H.K. Kwon, H.S. Chang, Y.W. Park, Improvement of impact toughness of the SA 508 class 3 steel for nuclear pressure vessel through steel-making and heat-treatment practices, *Nucl. Eng. Des.* 174 (1997) 51–58.
- [12] K.-H. Lee, M.-C. Kim, W.-J. Yang, B.-S. Lee, Evaluation of microstructural parameters controlling cleavage fracture toughness in Mn–Mo–Ni low alloy steels, *Mater. Sci. Eng. A* 565 (2013) 158–164.
- [13] B. Sang, X. Kang, D. Li, A novel technique for reducing macrosegregation in heavy steel ingots, *J. Mater. Process. Technol.* 210 (2010) 703–711.
- [14] E.J. Pickering, H.K.D.H. Bhadeshia, Macro-segregation and microstructural evolution in a pressure-vessel steel, *Metall. Mater. Trans. A* 45 (2014) 2983–2997.
- [15] C. Zhou, R. Priestner, The evolution of precipitates in Nb-Ti microalloyed steels during solidification and post-solidification cooling, *ISIJ Int.* 36 (1996) 1397–1406.
- [16] R.M. Kuziak, Y.-W. Cheng, Microstructural evolution in microalloyed medium-carbon forging steels during thermomechanical processing steels During thermo-mechanical processing, *Proceedings of the International Conference on Processing, Microstructure and Properties of Microalloyed and Other Modern High Strength Low Alloy Steels*, 1992, pp. 51–66.
- [17] W.C. Leslie, R.L. Rickett, C.L. Dotson, C.S. Walton, Solution and precipitation of aluminum nitride in relation to the structure of low carbon steels, *Trans. ASM* 46 (1954).
- [18] R.C. Kerr, A.W. Woods, M.G. Worster, H.E. Huppert, Disequilibrium and macro-segregation during solidification of a binary melt, *Nature* 340 (1989) 357–362.
- [19] G. Lesoult, Macro-segregation in steel strands and ingots: characterisation, formation and consequences, *Mater. Sci. Eng. A* 413–414 (2005) 19–29.
- [20] J. Kowalski, J. Pstruś, S. Pawlak, M. Kostrzewa, R. Martynowski, W. Wołczyński, Influence of the Reforging Degree on the Annihilation of the Segregation Defects in the Massive Forging Ingots, *Archives of Metallurgy and Materials*, 56 (2011).
- [21] A. Loucif, E.B. Fredj, N. Harris, D. Shahriari, M. Jahazi, L.P. Lapiere-Boire, Evolution of A-type macrosegregation in large size steel ingot after multistep forging and heat treatment, *Metall. Mater. Trans. B* (2018) 1–10.
- [22] C. Ji, G. Li, C. Wu, M. Zhu, Design and application of CSC-roll for heavy reduction of the bloom continuous casting process, *Metall. Mater. Trans. B Process Metall. Mater. Process. Sci.* 50 (2018) 110–122.
- [23] C. Zhang, D. Shahriari, A. Loucif, H. Melkonyan, M. Jahazi, Influence of thermo-mechanical shrinkage on macrosegregation during solidification of a large-sized high-strength steel ingot, *Int. J. Adv. Manuf. Technol.* 99 (2018) 3035–3048.
- [24] D. Li, X.Q. Chen, P. Fu, X. Ma, H. Liu, Y. Chen, Y. Cao, Y. Luan, Y. Li, Inclusion flotation-driven channel segregation in solidifying steels, *Nat. Commun.* 5 (2014) 5572.
- [25] Y.F. Cao, Y. Chen, D.Z. Li, Formation mechanism of channel segregation in carbon steels by inclusion flotation: X-ray microtomography characterization and multi-phase flow modeling, *Acta Mater.* 107 (2016) 325–336.
- [26] H. Ji, C. Ren, Y. Wang, Y. Guo, X. Zhang, H. Wang, Y. Zhu, The evolution of strain pattern induced by banded structure under uniaxial tension in low-carbon microalloyed steel, *Mater. Sci. Eng. A* 748 (2019) 253–261.
- [27] A.A. Korda, Y. Mutoh, Y. Miyashita, T. Sadasue, S.L. Mannan, In situ observation of fatigue crack retardation in banded ferrite-pearlite microstructure due to crack branching, *Scr. Mater.* 54 (2006) 1835–1840.
- [28] L. Shi, Z. Yan, Y. Liu, X. Yang, Z. Qiao, B. Ning, H. Li, Development of ferrite/bainite bands and study of bainite transformation retardation in HSLA steel during continuous cooling, *Met. Mater. Int.* 20 (2014) 19–25.
- [29] A. Ramazani, H. Quade, M. Abbasi, U. Prah, The effect of martensite banding on the mechanical properties and formability of TRIP steels, *Mater. Sci. Eng. A* 651 (2016) 160–164.
- [30] B.L. Ennis, C. Bos, M.P. Aarnts, P.D. Lee, E. Jimenez-Melero, Work hardening behaviour in banded dual phase steel structures with improved formability, *Mater.*

- Sci. Eng. A 713 (2018) 278–286.
- [31] F.A. Khalid, M. Farooque, A. Ul Haq, A.Q. Khan, Role of ferrite/pearlite banded structure and segregation on mechanical properties of microalloyed hot rolled steel, *Mater. Sci. Technol.* 15 (2013) 1209–1215.
- [32] X. Zhang, Y. Wang, J. Yang, Z. Qiao, C. Ren, C. Chen, Deformation analysis of ferrite/pearlite banded structure under uniaxial tension using digital image correlation, *Opt. Lasers Eng.* 85 (2016) 24–28.
- [33] C.C. Tasan, J.P.M. Hoefnagels, M.G.D. Geers, Microstructural banding effects clarified through micrographic digital image correlation, *Scr. Mater.* 62 (2010) 835–838.
- [34] C. Ren, X. Zhang, H. Ji, N. Zhan, Z. Qiao, Effect of banded morphology and grain size on the tensile behavior of acicular ferrite in HSLA steel, *Mater. Sci. Eng. A* 705 (2017) 394–401.
- [35] Y. Shao, C. Liu, Z. Yan, H. Li, Y. Liu, Formation mechanism and control methods of acicular ferrite in HSLA steels: a review, *J. Mater. Sci. Technol.* 34 (2018) 737–744.
- [36] *Failure Analysis and Prevention*, 11 (2002) 5–81.
- [37] C. Zhang, A. Loucif, M. Jahazi, R. Tremblay, L.-P. Lapierre, On the effect of filling rate on positive macrosegregation patterns in large size cast steel ingots, *Appl. Sci.* 8 (2018) 1878.
- [38] M. Hunkel, J. Kagathara, U. Prah, The Influence of Segregations after Forming on the Heat Treatment Result of Bevel Gears, *Steel Research International*, (2019), p. 1800427.
- [39] D. Xu, C. Cerbu, H. Wang, I.C. Rosca, Analysis of the hybrid composite materials reinforced with natural fibers considering digital image correlation (DIC) measurements, *Mech. Mater.* 135 (2019) 46–56.
- [40] H. Wang, C.J. Boehlert, Q.D. Wang, D.D. Yin, W.J. Ding, In-situ analysis of the tensile deformation modes and anisotropy of extruded Mg-10Gd-3Y-0.5Zr (wt.%) at elevated temperatures, *Int. J. Plast.* 84 (2016) 255–276.
- [41] C. Örnek, D.L. Engelberg, An experimental investigation into strain and stress partitioning of duplex stainless steel using digital image correlation, X-ray diffraction and scanning Kelvin probe force microscopy, *J. Strain Anal. Eng. Des.* 51 (2016) 207–219.
- [42] J. Kadkhodapour, A. Butz, S. Ziaei-Rad, S. Schmauder, A micro mechanical study on failure initiation of dual phase steels under tension using single crystal plasticity model, *Int. J. Plast.* 27 (2011) 1103–1125.
- [43] S. Wang, C. Li, L. Han, H. Zhong, J. Gu, Visualization of microstructural factors resisting the crack propagation in mesosegregated high-strength low-alloy steel, *J. Mater. Sci. Technol.* 42 (2020) 75–84.
- [44] C.W. Li, L.Z. Han, X.M. Luo, Q.D. Liu, J.F. Gu, Effect of tempering temperature on the microstructure and mechanical properties of a reactor pressure vessel steel, *J. Nucl. Mater.* 477 (2016) 246–256.
- [45] J. Deng, J. Ma, Y. Xu, Y. Shen, Effect of martensite distribution on microscopic deformation behavior and mechanical properties of dual phase steels, *Jinshu Xuebao/Acta Metall. Sin.* 51 (2015) 1092–1100.
- [46] C. Li, L. Han, G. Yan, Q. Liu, X. Luo, J. Gu, Time-dependent temper embrittlement of reactor pressure vessel steel: correlation between microstructural evolution and mechanical properties during tempering at 650 °C, *J. Nucl. Mater.* 480 (2016) 344–354.
- [47] S. Gao, C.S. Wu, G.K. Padhy, L. Shi, Evaluation of local strain distribution in ultrasonic enhanced Al 6061-T6 friction stir weld nugget by EBSD analysis, *Mater. Des.* 99 (2016) 135–144.